PHYSICAL REVIEW B **92**, 104427 (2015)

Electronic, magnetic, transport, and thermal properties of single-crystalline UFe_2Al_{10}

R. Troć,[1] M. Samsel-Czekała,[1] E. Talik,[2] R. Wawryk,[1] Z. Gajek,[1] and M. Pasturel[3]
[1]*W. Trzebiatowski Institute of Low Temperature and Structure Research, Polish Academy of Sciences, Okólna 2, 50-422 Wrocław, Poland*
[2]*A. Chełkowski Institute of Physics, University of Silesia, Uniwersytecka 4, 40-007 Katowice, Poland*
[3]*Institut des Sciences Chimiques de Rennes, Chimie du Solide et Matériaux, Université Rennes 1, UMR CNRS 6226, Campus de Beaulieu, 263 av. Général Leclerc, 35042 Rennes Cedex, France*

(Received 26 June 2015; revised manuscript received 12 August 2015; published 24 September 2015)

The valence and core-level x-ray photoemission spectra (XPS), performed on an UFe_2Al_{10} single crystal, were measured using the Al $K\alpha$ radiation. The results of valence XPS show practically two separate regions of spectral intensity, one just at the Fermi level (E_F) and the other one being a wide content with its maximum at about 0.8 eV below E_F. These give rise to two electronic configurations of the $5f$ states in the studied aluminide, itinerant and localized ones, i.e., their *dual* character. In such a situation the corresponding valence spectra, calculated within the local density approximation (LDA), well explain the former configuration, being responsible for a metallic behavior of the studied compound. Moreover, this behavior is confirmed clearly also by our results of magnetotransport measurements. On the other hand, the obtained magnetic susceptibility, specific heat, electrical resistivity, and thermoelectric power data support very well the local character of the $5f^2$-electron configuration of the U^{4+} ion in UFe_2Al_{10} having the orthorhombic and cage-type crystal structure. Based on that configuration, the magnetic and thermal characteristics of the compound were modeled by the effective crystal field (CF) potential in the intermediate coupling scheme using initial parameters obtained by the angular overlap model (AOM). The obtained final CF parameters yielded the CF level scheme, composed of only singlets, proper for orthorhombic symmetry. Such a set of singlets reproduces in a satisfactory way both the strongly anisotropic temperature variations of the magnetic susceptibility, measured along the three main crystallographic directions, as well as the Schottky anomaly, evaluated using specific heat results of isomorphic $ThFe_2Al_{10}$ as a phonon reference. Also, the strongly anisotropic behavior of the Seebeck coefficient and its low temperature maxima observed for the compound studied here have been explained roughly by the CF effect.

DOI: 10.1103/PhysRevB.92.104427 PACS number(s): 79.60.−i, 71.20.−b, 75.47.−m, 72.15.Jf

I. INTRODUCTION

Detailed studies of the U-Fe-Al system have shown the existence of several ternary intermetallics in this system [1]. Among the most intensively investigated phases are those with a generalized formula UFe_xAl_{12-x}. At 1123 K an extended solid solution from $x = 3$ to $x = 7$ crystallizes in the tetragonal $ThMn_{12}$-type or its ordered $CeMn_4Al_8$ variant ($I4/mmm$ space group) [2]. Four magnetic regions have been identified in the compositional range $3.8 \leqslant x \leqslant 5.8$ [3]. This wealth of magnetic phases in such a broad homogeneity range is attributed to magnetic interactions between the uranium and iron sublattices. Decreasing the iron content down to $x = 2$ (UFe_2Al_{10}) results in the formation of the orthorhombic $YbFe_2Al_{10}$-type lattice ($Cmcm$ space group) [4]. Nevertheless, the crystal structure of the latter aluminide is closely related to that of the former ones [5,6]. In the $YbFe_2Al_{10}$ structure type, described by Niemann and Jeitschko [7], the uranium atom has a coordination number (CN) of 20 (4Fe + 16Al), while the iron atom forms a distorted icosahedron having 2 U and 10 Al atoms. Both types of coordination polyhedra are also characteristic of the crystal structure of UFe_4Al_8 and the difference between both structures arises from their different packing in the unit cells [6]. However, there is no direct subgroup relation between these two types of structures. Based on comparative analysis of the energies and using density functional theory (DFT) calculations, Zenou *et al.* [8] have explained why UFe_2Al_{10} adopts the $YbFe_2Al_{10}$-type structure rather than the $ThMn_{12}$ one. The crystallographic and electronic structures of UFe_2Al_{10} were also studied under applied pressure by Halevy *et al.* [9]. No pressure-induced change in applied pressure up to 23.6 GPa was reported for this phase. Their band structure calculations made at ambient and maximum applied pressure, using the full potential linearized augmented plane wave (LAPW) method, have shown that the partial $5f$ peak is located above the Fermi energy E_F and its density of state (DOS) is slightly shifted towards higher energies and simultaneously lowered by the pressure.

Furthermore, the title uranium phase exhibits a modified Curie-Weiss behavior and appeared to be a magnetically nonordered compound, as established by magnetization and neutron-diffraction measurements on polycrystalline samples down to 5 and 3 K, respectively [5,9]. Interestingly, the ^{57}Fe Mössbauer spectroscopy of UFe_2Al_{10} revealed an unusually high isomer shift for iron in this compound and confirmed the lack of a magnetic order [5]. Recently the temperature dependent susceptibility $\chi_i(T)$ of UFe_2Al_{10} and URu_2Al_{10} measured on single crystals along $i = a,b,$ and c axes has been reported [10], confirming the absence of magnetic ordering in both these aluminides at least down to 2 K. Strong anisotropy in measurements of $\chi_i(T)$ was observed along three axes. For example, $\chi_i(T)$ for UFe_2Al_{10} measured along the a and c axes exhibit a broad shoulder below 100 K prior to a fairly sharp increase below 20 K, while measurements along the b axis resulted in almost a temperature-independent Pauli paramagnetic behavior. Based on the above measurements, the authors of Ref. [10] have established for two above compounds, i.e., those based on Fe and Ru atoms, that $\chi_c > \chi_a > \chi_b$.

Among the isostructural family of rare-earth ternaries RT_2Al_{10}, those with $R = Ce$ and $T = Fe$, Ru, and Os, attracted in the past much interest because of having some exotic properties as, e.g., Kondo-semiconducting ones [11]. In addition, $CeFe_2Al_{10}$ was found to be a mixed valence compound [11–15], while $CeRu_2Al_{10}$ and $CeOs_2Al_{10}$ exhibit unconventional antiferromagnetic ordering with unexpectedly high Néel temperatures [11,15–17]. Their strong anisotropic behavior in the paramagnetic state reveals the presence of a strong hybridization between $4f$ and conduction electrons (f-c) acting together with a strong single ion anisotropy arising from the crystal field (CF) effect. However, quite similar to the UT_2Al_{10} series, nonordered Curie-Weiss properties down to the lowest temperatures studied were found in the family of the RFe_2Al_{10}-type ternaries, e.g., when $R =$ Ce, Pr, or Nd [12]. It is interesting to add that $YbFe_2Al_{10}$ [12,18,19] and $YbOs_2Al_{10}$ [20] are also classified as mixed valence compounds. For $R =$ Y and La, the first report [12] indicated a Pauli-paramagnetic behavior and the absence of a magnetic moment on iron atoms. Further investigations on YFe_2Al_{10} [18,19,21,22] converged to opposite conclusions and an effective magnetic moment of about $0.5\mu_B$ was attributed to Fe atoms. The divergences in the susceptibility and specific heat indicate that YFe_2Al_{10} is located near a quantum critical point and no magnetic order is observed down to 0.09 K [22].

Despite the large R-R distances (above 0.5 nm), all the remaining representatives of the RFe_2Al_{10} family with $R =$ Sm and Gd–Tm have been reported to be magnetically ordered with fairly high transition temperatures $T_t < 20$ K [12].

In order to better understand the behavior of UFe_2Al_{10} and compare it to the other members of the isostructural family, including URu_2Al_{10} [10,23,24], single crystals have been grown and investigated by means of magnetic, (magneto)electrical, thermopower, and specific heat measurements. In addition, an x-ray photoelectron spectroscopy (XPS) was performed and interpreted by results of our *ab initio* electronic structure calculations using the fully relativistic full-potential local-orbital (FPLO) method within the local density approximation (LDA). The aim of this paper is to present and discuss the obtained results for UFe_2Al_{10} compared to the recently published data for some selected rare-earth Fe-based aluminides, RFe_2Al_{10}. Moreover, taking advantage that the studied by us U-based aluminide is a paramagnet to the lowest temperature studied, i.e., the lack of an additional factor, we present here an interesting example of uranium intermetallic having the $5f$ electrons which exhibit a *dual* character, i.e., manifesting a coexistence of localized and itinerant characters. Thus, such a nature of the $5f$ states was theoretically discussed and documented experimentally in the past by a number of authors (for instance see Ref. [25] and references therein).

II. EXPERIMENTAL DETAILS

The UFe_2Al_{10} and reference $ThFe_2Al_{10}$ single crystals were prepared by the molten aluminum flux technique. Pure elements (all purities above 99.5%) with an atomic concentration ratio 1U:2Fe:49Al and 1Th:2Fe:49Al were premelted in an arc furnace to ensure a good repartition of the elements in the starting material. The resulting ball was placed in an alumina crucible and sealed in an argon cleaned evacuated quartz tube. The temperature was increased from 298 to 1323 K in 6 h, left at this temperature for 24 h, and then cooled down to 933 K at a rate of $1\,K\,h^{-1}$. The tubes were removed from the furnace at this temperature and left in air until they reach room temperature (RT). The excess aluminum was removed by etching in diluted hydrochloric acid. The obtained single crystals have a platelike shape with a typical size of approximately $2 \times 1 \times 0.3\,mm^3$. Their chemical composition and their crystallographic quality and orientation were carried out by both SEM-EDS and the x-ray diffraction techniques. No impure phase was observed by an x-ray analysis. The deduced cell parameters are exactly fitting to the ones previously reported by Noël *et al.* [5] or Sugai *et al.* [10]. Most of the crystals presented the a crystal axis perpendicular to the plate base. As will be described below, we were also able to obtain fairly large U-based single crystals up to approximately $0.5\,cm^3$ having well-formed facets (Fig. 1). They were used in photoemission and specific heat measurements. The lattice parameters of $ThFe_2Al_{10}$ were found to be $a = 0.9017$ nm, $b = 1.0293$ nm, and $c = 0.9116$ nm.

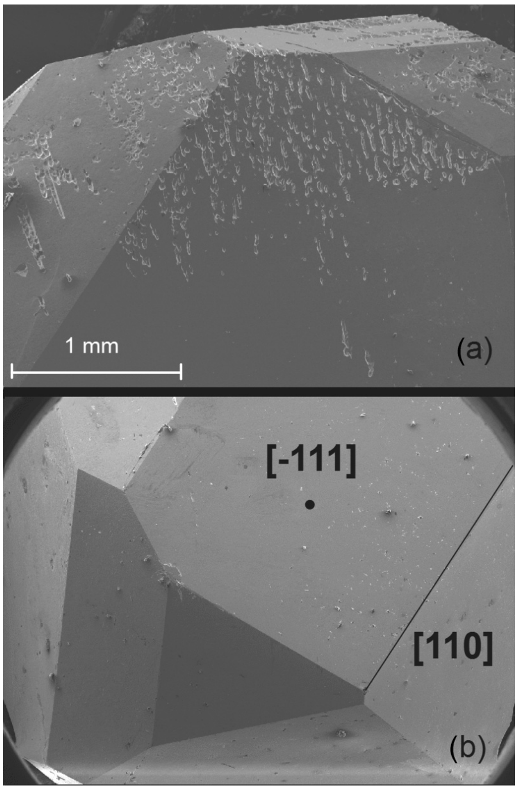

FIG. 1. Electron microscope images of the UFe_2Al_{10} single crystal, presented in two different orientations (a) and (b). Note that some facets are marked by the Miller indexes.

The overall XPS spectrum of UFe_2Al_{10} was recorded in a broad range of 0−1400 eV binding energy (BE) with monochromatized Al $K\alpha$ ($h\nu = 1486.6$ eV) x-ray radiation at RT, employing a PHI 5700 ESCA spectrometer. The single crystal of a suitable size was repeatedly cleaved *in situ* about every 10 min under high vacuum (UHV) conditions of 5×10^{-10} Torr immediately before each measurement. The oxide and carbon contamination was examined by monitoring the intensity of the O 1s (531 eV BE) and C 1s (285.0 eV BE) photoemission peaks weakly visible on the total XPS spectrum. Hence, the sample was negligibly contaminated by oxygen or carbon. The Fermi level ($E_F = 0$) was referred to the $4f_{7/2}$ level of gold at 84.0 eV BE. The energy spectrum of emitted electrons was analyzed by a hemispherical mirror analyzer with an energy resolution of about 0.3 eV. A standard procedure of subtracting the background with the use of the Tougaard method [26] was followed by a deconvolution of the total core-level curve utilizing the Doniach-Šunjić-type expression [27].

For electrical resistivity measurements the samples in the form of bar-shaped specimens were cut from the irregular platelike single crystal with the dimension of about $1.5 \times 0.4 \times 0.3\,\mathrm{mm}^3$ along the a direction and of $1.5 \times 0.6 \times 0.3\,\mathrm{mm}^3$ along the b and c directions. The electrical contacts (four points) were done by the electrochemical deposition of Cu and finally silver thin wires were glued by using a silver paste. The measurements were carried out in a ^{3}He cryostat in the temperature range 0.3–300 K, using an ac method. On the same samples the magnetoresistivity was measured in applied fields up to 9 T. A homemade setup [28] was used for the thermoelectric power measurements at temperatures from 0.4 K to 300 K. The frontal surfaces of the same samples along the a, b, and c directions were wetted with the liquid In-Ga alloy in order to improve the thermal and electrical contacts with chamber plates after removal of the copper electrical contacts.

The specific heat of the single-crystalline samples of UFe_2Al_{10} and $ThFe_2Al_{10}$ with masses of 49.5 and 29.2 mg, respectively, was measured by thermal relaxation method in a commercial Quantum Design PPMS platform in the temperature range 2–300 K. The samples were glued to the holder using Apiezon N vacuum grease which addenda were measured earlier. The specific heat of the UFe_2Al_{10} single crystal was also measured in magnetic fields varied from 0.5 to 9 T applied parallel to the a axis.

III. CALCULATION DETAILS

The nonmagnetic band structure of UFe_2Al_{10} has been calculated by the fully relativistic version of the FPLO method [29]. In this approach all electrons are treated by the four-component Kohn-Sham-Dirac equation, containing implicitly all relativistic effects including spin-orbit (SO) coupling, being solved self-consistently. The Perdew-Wang parametrization [30] of the LDA exchange-correlation potential was employed. The experimental values of both the lattice parameters, $a = 0.89146$ nm, $b = 0.101986$ nm, $c = 0.90114$ nm (close to those of our crystal), and atomic positions in the orthorhombic unit cell (u.c.) of the $YbFe_2Al_{10}$-type ($Cmcm$, space group no. 63) were used from Ref. [5]. Except for one position of the U atom in 4c and Fe atom in 8d, there are as many as five different positions of Al, namely Al(1) and Al(2) in 8g, Al(3) and Al(4) in 8f, and Al(5) in 8e. Note that the central position of the U atom (in 4c) in this cage-type structure is unique. Furthermore, the U atoms form one dimensional (1D) zigzag chains. However, the shortest U-U distance (0.5184 nm) in this system exceeds considerably the Hill limit and, hence, is too large for any direct U-U interactions [5].

In our calculations the valence basis sets were used as follows: the U $5s5p5d$; $6s6p$ (pseudocore) and $6d$; $5f$; $7s7p$ (pure valence); Fe $3s3p$ (pseudocore) and $3d$; $4s4p$ (pure valence); Al $2s2p$ (pseudocore) and $3s3p3d$ (pure valence) states. The size of the $\boldsymbol{k}$-point mesh in the irreducible wedge of the Brillouin zone (BZ) was $8 \times 8 \times 8$ (105 points). The atomic-orbital based FPLO method provides the Mulliken decomposition of charges, which is somewhat dependent on the orbitals used.

The total and partial densities of states (DOSs) and Fermi surface (FS) have been computed. The partial DOSs were determined for different atomic sites (in the u.c.) or electron orbitals and are presented per formula unit (f.u.). For comparison with the experimental XPS spectra, the corresponding theoretical valence band XPS spectrum was simulated by the standard procedure. Namely, the partial DOSs for different electron orbitals of the constituent atoms were multiplied by the respective weight factors proportional to atomic subshell photoionization cross sections, tabulated in Ref. [31]. The outputs were summed up and convoluted with a Gaussian of a full width at the half maximum (FWHW) being equal to 0.3 eV to simulate the energy resolution of the experimental analyzer. Because the XPS spectrum was determined based on the cross sections, given in Ref. [31] up to two significant digits, the overall accuracy of the spectrum intensity is not better than several percent. However, only relative XPS intensities of the peaks could be affected by the inaccuracy of the cross sections used in the calculations and not their locations on the BE scale.

IV. RESULTS AND DISCUSSION

A. Electronic structure

1. DOS and Fermi surface

The fully relativistic total and partial DOSs of UFe_2Al_{10}, calculated within LDA, are plotted in Fig. 2(a) and the corresponding Fermi surface is displayed in Fig. 3. As indicated by the relatively low DOS at E_F and the FS containing not large closed holelike and electronlike pockets (see below), UFe_2Al_{10} exhibits rather a weakly metallic behavior in accord with our temperature dependent transport measurements described later on. The two Kramers double-degenerate bands, numbered as 347 and 349, crossing E_F, are dominated by the contribution of the U $5f_{5/2}$ states, separated by a valley from the contribution of unoccupied U $5f_{7/2}$ states, the latter being centered at about 0.75 eV above E_F (their SO splitting is of 0.75 eV) as depicted in Fig. 2(a).

The U $5f_{5/2}$ states form a unique structure consisting of six narrow subpeaks [numbered as 1–6 in the inset to Fig. 2(a)], These states are strongly hybridized with the remaining states, i.e., U $6d$ (not displayed), Fe $3d$, and Al $3sp$. The latter states originate from all five aluminum atomic sites in the u.c.

All the constituent atoms of UFe_2Al_{10}, which form a cage-type configuration, create the metalliclike bond, similarly to the case of isostructural (U;Ce)Ru_2Al_{10} systems [24]. Except for the sharp U $5f$ peaks located around E_F, there exists also a tail contribution from these states [see hatched area in Fig. 2(a)], ranging to about 3.0 eV below E_F. As seen in the inset to Fig. 2(a), the Fermi level is situated just between the

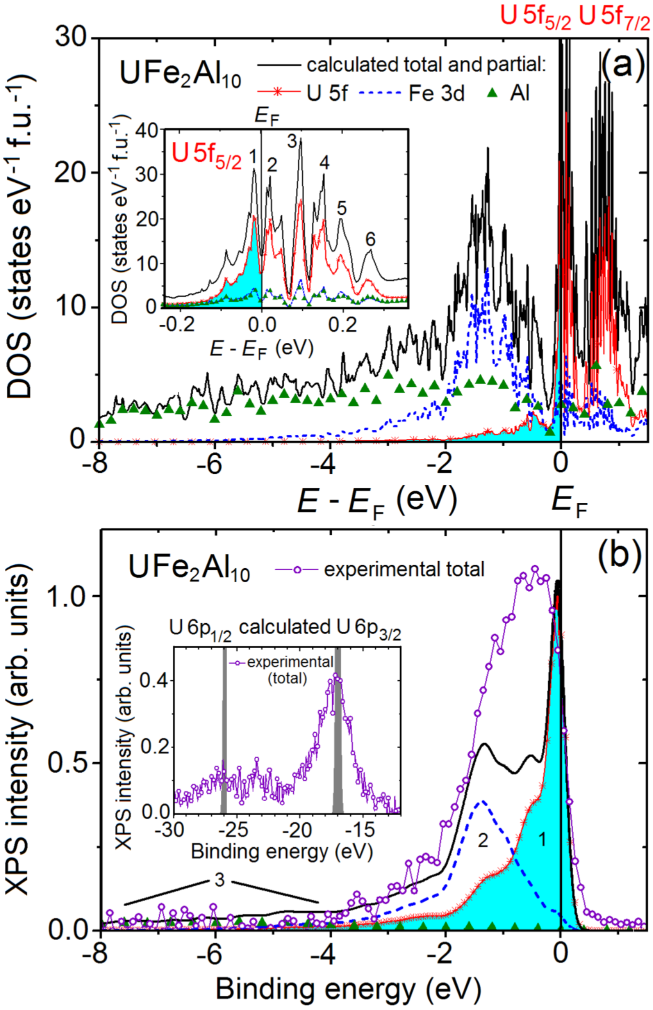

FIG. 2. (Color online) (a) Calculated (LDA) total and partial DOSs of UFe_2Al_{10}. The inset shows the same in the vicinity of E_F and in the extended DOS scale. (b) Valence band XPS of UFe_2Al_{10}: total experimental and corresponding calculated total and partial spectra. The inset shows experimental and calculated pseudo-core U $6p_{1/2}$ and U $6p_{3/2}$ lines.

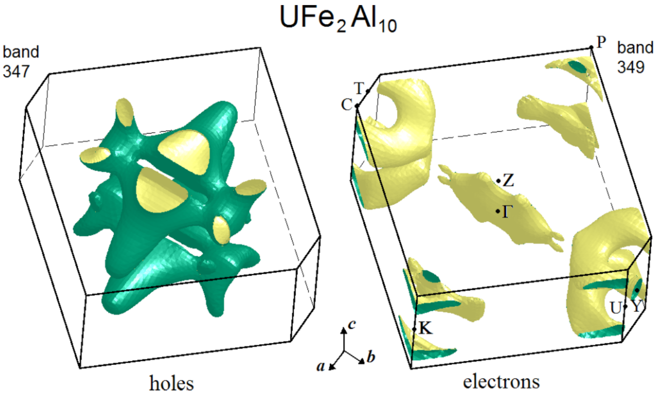

FIG. 3. (Color online) Calculated (LDA) FS sheets of UFe_2Al_{10}, existing in two Kramers double-degenerate bands (nos. 347, 349). They are drawn separately within the BZ boundaries. Dark (green) and light (yellow) colors visualize the inside (electrons) and outside (holes) of FS, respectively.

subpeaks 1 and 2, yielding the calculated Sommerfeld coefficient $\gamma_b = 27.2\ \mathrm{mJ\,mol^{-1}\,K^{-2}}$, being in very good agreement with its experimental value $\gamma_0 = 28(1)\ \mathrm{mJ\,mol^{-1}K^{-2}}$ reported below and suggesting weak electron-electron correlation. Interestingly, the computed electron occupation number (per one atom) for the U $5f$ electrons in UFe_2Al_{10} amounts to 2.9, being close to that of a free atom (3). Meanwhile, the U $6d$ and Fe $3d$ electrons have enhanced their numbers, 2.4 (1) and 7.1 (6), respectively. The Al $3spd$ states, coming from five nonequivalent atomic positions, form a broad structure in the whole range of the valence and conduction bands [see Fig. 2(a)]. In turn, the Fe $3d$ states exhibit a pronounced multipeak structure ranging from -6.0 eV to E_F with a maximum at about -1.5 eV and a long tail spreading well above E_F. Moreover, there is a hybridization U $5f$-Fe $3d$ dip visible in the total DOS at -0.25 eV [see Fig. 2(a)]. Our overall DOS of UFe_2Al_{10} is in good agreement with that obtained for this system by Halevy *et al.* (see Fig. 5 of Ref. [9]) but employing a different full potential LAPW method and only in the scalar relativistic mode, which yielded one (instead of two) broad U $5f$ peak with its majority part located just above E_F. In turn, our DOS is hard to compare with that reported by Zenou *et al.* (Fig. 8 of Ref. [8]) obtained by fully relativistic and full potential LAPW but in the spin-polarized GGA mode and displayed separately for spin-up and spin-down channels. Interestingly, our U $5f$ contribution to DOS of UFe_2Al_{10} is completely different as to both its shape and location from that of the isostructural URu_2Al_{10} obtained with the same method in Ref. [24].

From the computed Fermi surface of UFe_2Al_{10}, which is presented in Fig. 3, one can see that it consists of three-dimensional holelike and electronlike closed pockets, originating from the 347th and 349th bands, respectively. These FS sheets possess different anisotropic shapes and are located either around the Γ point or in the corners of the Brillouin zone (BZ). Their overall closed and two-type-carrier character is similar to that of an isostructural URu_2Al_{10} analog (Fig. 3 of Ref. [24]). However, in UFe_2Al_{10} both a lack of the extra sheet of 345 band, and a smaller volume of the remaining FS pockets, being different from those in the URu_2Al_{10} counterpart, reveal less metallic behavior in the considered Fe-based than Ru-based compound, in agreement with our transport data presented in the following sections.

2. *XPS spectra*

The computed total and main partial contributions of UFe_2Al_{10} and the corresponding experimental XPS valence band spectra are compared in Fig. 2(b). As shown, the overall theoretical spectrum of UFe_2Al_{10} contains three main contributions (1–3). In the spectrum, the first largest and narrowest peak crossing E_F, accompanied by two smaller peaks with higher BE (within the hatched area of peak 1), originates mainly from the U $5f_{5/2}$ states (dominating in the region from E_F to about 1 eV BE). In addition, this peak is also overlapped by a tail contribution from the Fe $3d$ electrons. These electrons form predominantly the second main contribution (2), centered at about 1.5 eV BE, which is also partly overlapped by the U $5f$ contribution (1). All these give rise to a marked hybridization between these two kinds of electron orbitals. At the same time, the contribution of the U 6*d* states is invisible in the intensity scale of Fig. 2(b) due to their low photoionization cross sections [31]. Hence, in practice, it cannot be detected by the XPS measurements. Similarly, the total contribution of Al atoms in UFe_2Al_{10}, though distinctly visible in Fig. 2(a), is strongly diminished by their photoionization cross sections [31], yielding the broad contribution (3). An observed complete lack of the O 2*s* line, usually occurring around 6 eV BE, signals practically the lack of contamination by oxygen in the sample (see Fig. 1). A similar effect has been observed in the overall spectrum of UFe_2Al_{10} (not shown), in which the O 1*s* peak at 531 eV BE was hardly seen. A microscopic analysis of this single crystal yielded the following content $U_{1.0(4)}Fe_{1.8(4)}Al_{10.1(0)}$.

As Fig. 2(b) indicates, the overall theoretical and experimental XPS spectra of UFe_2Al_{10} were normalized to average highest peak intensities around the Fermi level. As seen from this figure, there is some fairly large excess of intensities (extending in the region from E_F to 2 eV of BE) between the experimental and theoretical XPS spectra, the latter being characterized by a sharp, narrow peak situated just at E_F. This enhanced emission may be caused by the presence of some U 5*f* multiplets like those in UPd_3, as shown in Fig. 3 of Ref. [32]. It is clear that these multiplets cannot be reproduced by single-particle DOS calculations. To show this feature illustratively, we display in Fig. 4 an exemplary comparison between the U 5*f* spectra of UPd_3 and UNiSn obtained by the resonant U $5d \rightarrow 5f$ photoemission (RPES) technique (see Fig. 2 in Ref. [33]) and our 5*f* spectrum for UFe_2Al_{10} derived as described below. The former study allowed for determining the partial spectra weight (PSW), i.e., distributions of both the U 5*f* and *T d* electrons in the typically localized systems considered above [33] with the assigned $5f^2$ configuration. Especially the inelastic neutron scattering investigations confirmed well defined crystal field excitations in both these reference compounds [34,35]. In view of the lack of a possibility to apply an RPES technique in our case, we have simply subtracted the calculated Fe 3*d* contribution from the total experimental valence XPS data assuming some consistency of an expected experimental weight of the Fe 3*d* electrons with that of the theoretical one. As is apparent from Fig. 4, the 5*f* electron weights in UNiSn and UFe_2Al_{10} are quite comparable to each other. Also, the values of linear specific heat coefficients for both systems are close to each other (about 28 mJ $mol^{-1}K^{-2}$, see below). Based on what has been said above, we can also expect in UFe_2Al_{10} evidence of a CF splitting of a $J = 4$ multiplet, being consistent with the Hund's rule ground state of the $5f^2$ configuration as discussed here for the reference compounds [34,35].

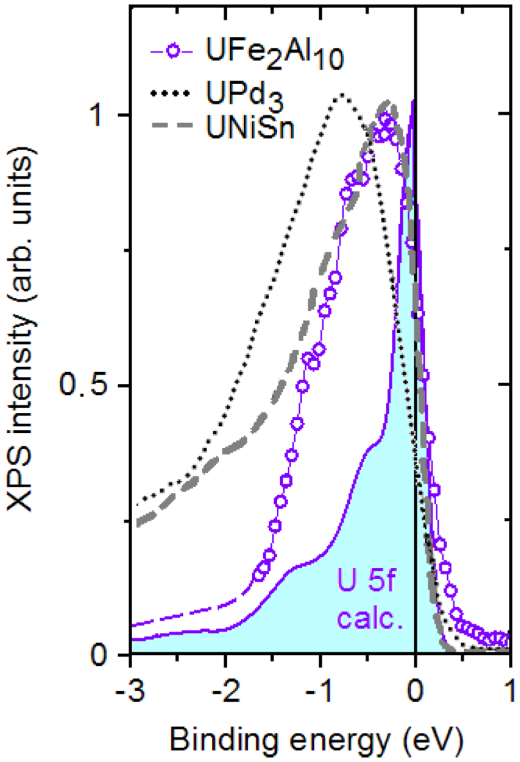

FIG. 4. (Color online) The comparison of the U 5*f*-part valence XPS of our UFe_2Al_{10} (experimental and calculated spectra) with those of UPd_3, UNiSn [33] obtained by RPES technique (see main text).

It is worth noting that the overall experimental valence XPS spectrum of UFe_2Al_{10} is narrower than that of its isostructural URu_2Al_{10} analog (see Fig. 4(a) of Ref. [24]) because the Fe 3*d* contribution is located much closer to the Fermi level than that of the Ru 4*d* electrons.

Furthermore, experimental broad pseudocore U $6p_{1/2}$ and U $6p_{3/2}$ XPS lines in UFe_2Al_{10} are plotted in the inset to Fig. 2(b). Interestingly, their positions, centered at 26 and 17 eV BE, respectively, are in good agreement with our corresponding calculated narrow lines and with those in other binary and ternary systems like UGe_2 [36], UCu_2Si_2 [37], and UPtSn [38].

The structure of the U 4*f* core lines in UFe_2Al_{10}, displayed in Fig. 5, yields some substantial information on the final states in the photoemission processes. These lines have been decomposed according to the Doniach-Šunjić theory [27] (after subtracting the background by the Tougaard method [26]), into two asymmetric $4f_{5/2}$ (388.5 eV BE) and $4f_{7/2}$ (377.5 eV BE) main sublines, being split by 11 eV due to the SO interaction. Both U $4f_{7/2}$ and $4f_{5/2}$ sublines are accompanied only by a single small-intensity symmetric satellite called 7-eV, characteristic of many uranium intermetallics. Such satellites were detected among others in UPd_3 [39,40] and UFe_4Al_8 [41], which indicates some localization effect of the U 5*f* electrons. In the former compound these satellites are located closer to the main lines, namely 6 eV BE higher. In UFe_2Al_{10} these satellites are centered at about 384.5 eV BE and 395.5 eV BE, i.e., at higher BE by 7.0 eV as indicated in Fig. 5. The small intensities of these peaks is likely a result of some overlapping by a broad plasmon contribution (centered at 396.0 eV BE with the extended tail), causing some troubles to their proper determination. It is interesting to note that in the case of URu_2Al_{10} there was observed also only one satellite so-called 1-eV [24]. In UFe_2Al_{10} the lack of both 1-eV and so-called 3-eV satellites (the latter around 380 eV BE) in the U 4*f* spectrum does not give an evidence of a mixed-valence behavior of the U 5*f* electrons. However, the difference (about 2 eV higher BE) in the final 5*f* states of the main lines between UPd_3 (see, e.g., Refs. [39,40]) and

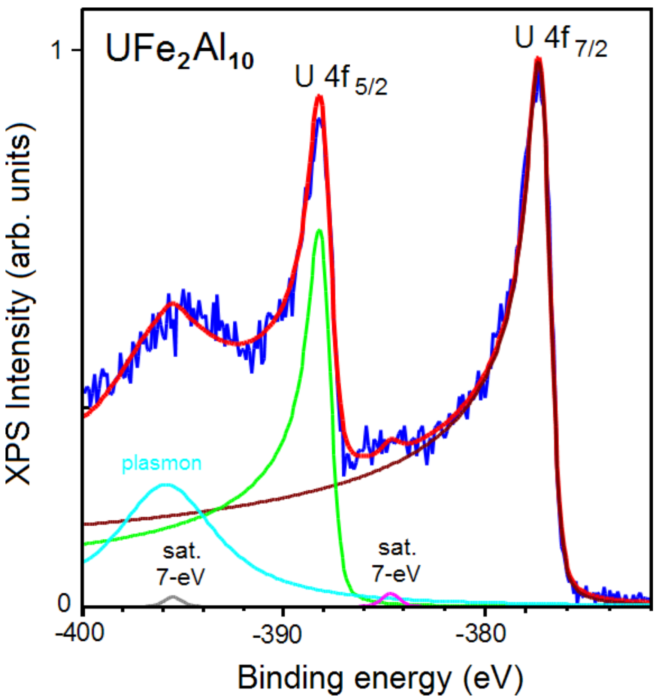

FIG. 5. (Color online) The experimental XPS of the U $4f$ core lines in UFe$_2$Al$_{10}$ measured on a single crystal. The lines are decomposed into the main sublines U $4f_{5/2}$ and U $4f_{7/2}$ and the symmetric satellites 7-eV. In addition, the U $4f_{5/2}$ subline is overlapped by the large plasmon contribution.

UFe$_2$Al$_{10}$ (see Fig. 5), which corresponds to a change of the final state from $5f^3$ to $5f^4$, respectively, is surprising in view of our interpretation of the susceptibility behavior of the latter aluminide given below. Nevertheless, a similar difference exists for a number of intermetallic uranium compounds, like UGa$_2$ [42], U$_2$Zn$_{17}$ [43], URu$_2$Si$_2$ [43], UCu$_2$Si$_2$ [37], UPt$_2$Si$_2$ [44], UPd$_2$Al$_3$ [45], and many others, despite the fact that for most of them a CF analysis has been interpreted by assuming the initial $5f^2$ electron configuration with the $J = 4$ (^{3}H$_4$) ground multiplet [46–52].

According to Beaux II *et al.* [39], the increased binding energy observed for the $4f$ core levels of UPd$_3$ might be caused by somewhat worse hole screening with respect to other uranium intermetallics, e.g., those mentioned above, including also UFe$_2$Al$_{10}$. Moreover, this fact is not associated exclusively with the effect of delocalization of the $5f$ electrons in the latter compounds. However, there is no doubt that the effect of $5f$-ligand hybridization plays a much more important role in the compounds considered above than in UPd$_3$, in which it is quite negligible [39,40].

Finally, we also mention the experimental core XPS spectra of the Fe $2p$ and Al $2p$ occurring with higher binding energies (not displayed here). For example, the Fe $2p$ lines are located at the same energies as those earlier measured for a family of the ternaries AFe$_4$Al$_8$, where $A =$ U,Th,Y, and Sc, i.e., at 720.2 (706.8) eV BE for the Fe $2p_{1/2}$ ($2p_{3/2}$) spectra. These energies are very close to those reported for pure iron. In turn, the high-intensity Al $2p$ line, centered at about 72.6 eV BE, is close to the corresponding pure aluminum line (72.9 eV BE) and also to the lines in AFe$_4$Al$_8$ defined above [41] and, e.g., in URu$_2$Al$_{10}$ [24]. Moreover, the Al $2p$ peak consists of two subpeaks having different intensities, being split by the SO interaction by about 0.5 eV.

B. Magnetic properties

1. Experimental magnetic susceptibility

Figure 6(a) shows the temperature-dependent susceptibility $\chi_i(T)$ measured along three crystallographic directions $i = a,b,c$. This dependence exhibits strong uniaxial magnetic anisotropy, for which the magnetization easy axis is the a axis, i.e., $\chi_a > \chi_c > \chi_b$. This finding is, however, different from that reported in Ref. [10], where the c axis was found to be the easy one, i.e., with $\chi_c > \chi_a > \chi_b$. Quite similarly, the $\chi_i(T)$ of CeFe$_2$Al$_{10}$ also exhibits uniaxial magnetic anisotropy and

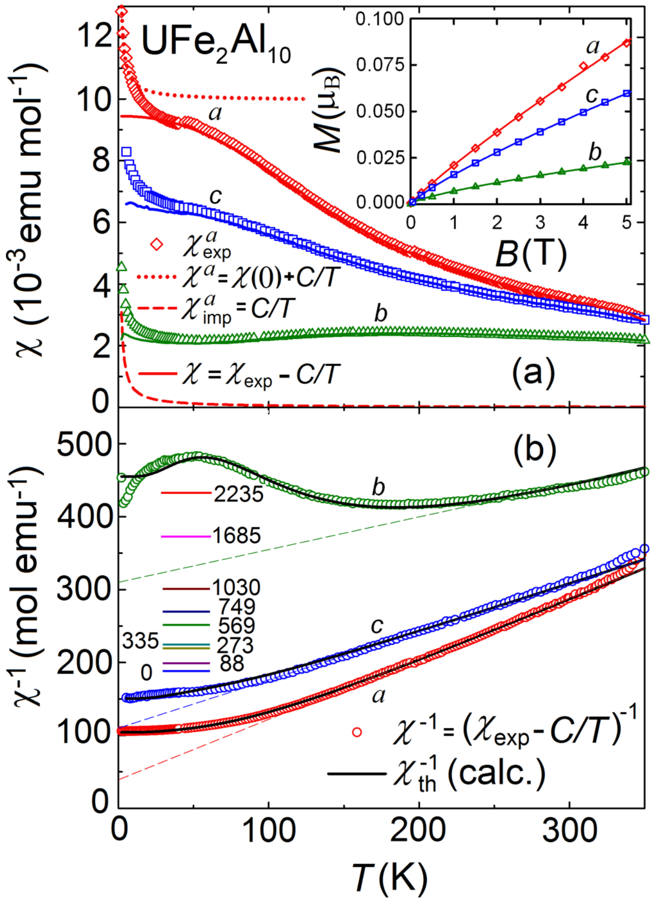

FIG. 6. (Color online) (a) Temperature dependencies of the susceptibility measured in the three main crystallographic directions of orthorhombic UFe$_2$Al$_{10}$. Low-temperature upturn in $\chi_i(T)$ (where $i = a,b,c$) is assumed to come from impurities which susceptibilities follow the Curie law. An example of the correction is presented in the figure by respective curves. In the inset, magnetization M versus magnetic field B taken at 2 K is shown. Note small curvatures of all three lines. (b) The corrected reverse susceptibility versus temperature (symbols) compared to those calculated (see text), marked by solid curves. Calculations based on the CF splitting of the ground multiplet (see scheme of the CF levels in units K), resulting for the $5f^2$-electron configuration of the U^{4+} ion in the considered here uranium-iron-aluminide.

TABLE I. The magnetic parameters of UFe_2Al_{10}.

Axis	$\chi_M^{300\,K}(10^{-3}$ emu mol$^{-1})$	θ_p(K)	μ_{eff}[a] (μ_B)
a	3.5	−45	3.08
b	2.3	−700	4.29
c	3.1	−160	3.38

[a] Any meaning of μ_{eff} requires measurements performed at considerably higher temperatures.

the susceptibility along the *a* axis have the highest values [16]. Both our and Sugai *et al.*'s [10] results show not only the smallest susceptibility values of the *b* axis compared to those of the other directions but also a weak temperature change below RT. In addition, our measurement taken along this axis yields a very broad susceptibility maximum around 200 K. In all cases it is clear that the susceptibilities below about 100 K reveal a tendency to saturation, which however is stopped by small χ tails starting below about 50 K to grow monotonically with lowering temperature. A similar behavior of the susceptibility at low temperatures was also reported by Sugai *et al.* We think that this upturn comes most likely from some impurities. Therefore, we have corrected the low temperature dependencies of our susceptibility curves by subtracting χ_{imp} (assuming its following the Curie law C/T) from the respective experimental values, to obtain finally approximately constant $\chi(0)$ saturated values for all three directions at $T = 0$ K. As an example, we present in Fig. 6(a) such a correction procedure for the susceptibility measured along the *a* axis. Thus, the reciprocal values of these corrected susceptibilities as a function of temperature are plotted in Fig. 6(b). The Curie-Weiss behavior for the three axes is given in Fig. 6(b) by the dashed lines. The corresponding magnetic parameters are listed in Table I. Note the large negative paramagnetic Curie temperatures, especially that along the *b* axis, which points out that it has not a physical meaning. In the next step we applied the crystal field theory on purpose to explain the observed highly anisotropic behavior of the susceptibility of UFe_2Al_{10}.

2. *Crystal field approach*

As shown in Sec. IV A 1, the spectral valence-band shape should be governed by the multiplet splitting of the U $5f$ electrons. This fact implies that the hybridization between conduction and $5f$ electrons (c-f) in UFe_2Al_{10} is rather small. Moreover, a lack of any magnetic or multipole orders in this aluminide, as observed down to 2 K, gives rise to a treatment of UFe_2Al_{10} as a prime candidate for the CF effects, which is a very rare feature among intermetallic uranium compounds. We can mention here, for example, another group of such compounds like U_2TSi_3 (where T = Fe, Ru, and Rh), for which a tendency of the susceptibility to saturate to a constant value at $T = 0$ K (singlet ground state) was also reported [53]. Interestingly that in UFe_2Al_{10} as well as in the U_2TSi_3 family, the *nd* shell is completely filled by the valence electrons of the uranium atom, which causes that this T content in the above intermetallics is nonmagnetic and one can make a CF approach based solely on the uranium ion.

The orthorhombic CF splits the $^3H_4$ ground multiplet of $U^{4+}(5f^2)$ into nine singlets. We model these states on the ground of the susceptibility measurements using the conventional Hamiltonian for the localized f electrons. It includes the on-site Coulomb repulsion and the spin-orbit correction represented respectively by the Slater integrals $F^k (k = 2,4,6)$ and the coupling coefficient ζ_{5f}, which all are kept constant. We apply the same values of these "free-ion" parameters as previously [50]. In the case of the uranium compound it is important that the free-ion interactions are then diagonalized simultaneously with the crystal field potential breaking the spherical symmetry [54,55]. The latter is varied to restore the temperature dependencies of the measured three components of the magnetic susceptibility. Because of relatively large number of the crystal field parameters (CFP) B_{kq} (nine: $k = 2,4,6; 0 \leqslant q \leqslant k$, even, all the parameters are real) in the orthorhombic symmetry, we use in the preliminary calculations a simplified CF model, namely, the angular overlap model (AOM). The obtained result is then refined in the second phase of the fitting in terms of the ordinary B_{kq} parameters. Details of the whole procedure are described elsewhere [50,56]. Hence, we show here only the relation between the CFP and AOM parameters,

$$B_{kq} = \sum_{t,\mu} W_{kq}^{\mu(t)} e_\mu^t, \tag{1}$$

where e_μ^t [$\mu = 0(\sigma), 1(\pi), 2(\delta); t = \text{Fe,Al}$] are the average energies of the metal-ligand interaction or metal-cell interaction in a general formulation of AOM based on the cellular partitioning [55,57]. These energies have the σ, π, and δ symmetries and play a role of adjustable parameters. The coordination coefficients $W_{kq}^{\mu(t)}$ absorb the whole information about the geometry of the coordination polyhedron (see Fig. 7) and the scaling factors $F^t(R_i^t, R_0^t) = (R_i^t/R_0^t)^{\gamma_\mu^t}$ characterizing the dependence of the energies on the metal-ligand (ML) distance: $e_\mu^t(R_i^t) \equiv e_\mu^t(R_0^t)F^t(R_i^t, R_0^t)$ [$e_\mu^t \equiv e_\mu^t(R_0^t)$]. The above power dependence may be regarded as general for ML distances varying in a restricted range within the coordination polyhedron. In what follows we use the power exponents determined by the squares of the ML overlap integral which were estimated for many f-electron systems (see Ref. [55] and the references therein). This is a consequence of the

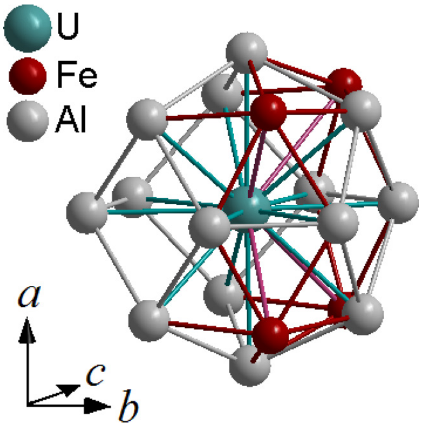

FIG. 7. (Color online) The reduced (CN = 18) coordination polyhedron of the U ion of UFe_2Al_{10} in the $YbFe_2Al_{10}$-type crystal structure, used in AOM calculations.

TABLE II. The AOM coordination coefficients $W_{kq}^{\mu(t)}$ in Eq. (1).

	Fe ($R_0 = 0.3413$ nm)			Al ($R_0 = 0.3185$ nm)		
kq	σ	π	δ	σ	π	δ
20	0.439	0.658	0.000	0.409	0.660	0.000
22	0.505	0.757	0.000	−0.154	−0.217	0.000
40	−2.203	−0.734	5.140	0.164	0.013	0.392
42	1.202	0.401	−2.805	−0.583	−0.167	0.860
44	−0.409	−0.136	0.954	0.842	0.265	−1.685
60	0.026	−0.039	0.016	2.189	−3.225	1.251
62	−0.397	0.595	−0.238	2.685	−3.962	1.543
64	−1.502	2.253	−0.901	−0.081	0.266	−0.203
66	−0.633	0.950	−0.380	0.355	−0.445	0.122

TABLE III. Two sets of the parameters B_{kq} (in K) obtained with and without AOM constraints as described in the main text.

B_{kq}	AOM	Refined
B_{20}	317	−561
B_{22}	−557	−304
B_{40}	5428	2977
B_{42}	−2216	−3064
B_{44}	−219	−1695
B_{60}	−8097	−11179
B_{62}	−7959	−1089
B_{64}	7425	8352
B_{66}	1737	−8470

assumption that the hybridization is the main crystal field mechanism for the type of compounds under consideration. Large CF effect justifies such an assumption if we remember that the effective hybridization contribution after suitable canonical transformation, e.g., the Schrieffer-Wolf transformation of the Anderson Hamiltonian, contains a difference between the Fermi energy and the ground state energy of the localized electrons in the denominator and if we take into account the XPS and DFT results presented in this paper. The crystal field parameters B_{kq} in Eq. (1) are normalized according to Wybourne's procedure [58]. As Fig. 7 indicates, there are 14 Al atoms with distances from 0.310 to 0.328 nm and four Fe atoms with distances 0.3413 nm, all from the uranium site. Two more Al(1) atoms (in 8g) have been omitted in the AOM calculations because of too far away distance (0.362 nm). Actually, we have two kinds of ligands, thus there are three e_μ^{Fe}(e_μ^{Al}) parameters for Fe (Al) ligands. The values of the corresponding $W_{kq}^{\mu(t)}$ coefficients gathered in Table II have been calculated using the crystallographic data from Ref. [5] and the power exponents γ_μ being equal to 6.1,7.3,9.3 for $\mu = 0,1,2$, respectively, which we have taken as typical for f-electron systems [55].

We fit the AOM parameters first and then the CF parameters to the experimental susceptibility data in three directions as a function of temperature using the Condon routine [59,60] adopted to the AOM approximation [61]. Previous studies [50,56,62] showed that the AOM parameters for this type of intermetallic materials are not so regular as for nonmetallic compounds [55,63]. Accordingly, a special procedure has been implemented. We start with the only one nonzero parameter among all six AOM parameters which gives the best fitting. Then we allow varying the next one, determined it in the same way. The procedure is repeated until all six final AOM parameters are obtained. Then, the result is converted to the B_{kq} parameters which, in turn, are used again as the starting ones in the refining calculations with the B_{kq} parameters being directly varied. Additionally, in each step we repeat the calculations for a number of random starting sets of relevant parameters to check whether the actual fitting error is indeed the smallest one and the solution is stable. This should minimize a risk of false minima caused by the large number of parameters in our model. It is worth mentioning some difficulty at that point. Namely, the orthorhombic CF parametrization is not unique in the sense that several completely different parameters sets which are able to describe the same sequence of eigenstates exist. This implies a standardization of the parameter sets in the refining. Because of the relatively low values of the second rank parameters, we apply the new standardization method based on the fourth-rank terms in the CF Hamiltonian (for details see Ref. [64]). The final set of the parameters is presented in Table III after transformation of the nominal coordinate system to the crystallographic one in which the AOM values are determined, to make the two sets *relatively* standardized.

The AOM parameters describing the U-Al and U-Fe interactions exhibit a certain similarity, both in values and signs: large and negative $e_\sigma = -1270$ K, -2703 K, positive $e_\pi = 1756$ K, 1311 K, and small and positive $e_\delta = 374$ K, 92 K for U-Al and U-Fe, respectively. It appears that the refined values of B_{kq} (shown in Table III) differ to some extent from their AOM estimates, which can be treated as a measure of the limited accuracy of the AOM approximation. They are considerably larger than in nonmetallic compounds suggesting an influence of a strong renormalization, which is insensitive to the screening by conduction electrons. The expected dominating role of the hybridization as signalized above finds a confirmation in our results. Of course one should be aware of crudeness of both the AOM and conventional (refined) CF parametrization for such a complex system. Nevertheless, it is not the first case when the oversimplified approach works better than its foundations indicate. We believe that our analysis can be a good starting point to a more sophisticated theoretical modeling accounting for either the many-electron CF approach or, preferably in the present case, the dynamic CF effect. Note that similarly large CF parameters have been reported previously for $\mathrm{CeRh_3Si_2}$ [62], $\mathrm{UGe_2}$ [56], and $\mathrm{UCu_2Si_2}$ [50].

The sequence of CF levels obtained from the fitting is shown in Fig. 6(b) and the composition of the wave functions are given in Table IV. Despite relatively high absolute values of CF parameters, the splitting of the $^3\mathrm{H}_4$ ground multiplet is rather moderate (2235 K), which can be attributed to the high coordination number, CN = (4Fe + 14Al) = 18. In addition, a mutual canceling of the fourth and sixth rank CF components seems to be at stake. The first excited level at 88 K, which is magnetically strongly coupled to the ground singlet ($|\langle 1|J_x|2\rangle| \sim 1$), is responsible for the broad maximum observed in the hard direction of the magnetic susceptibility

TABLE IV. The electronic states of the localized electron subsystem (C_{2v} point group) obtained using refined parameters listed in Table III.[a]

Irrep.	Energy (K)	Main components of the eigenstates (>0.1)
$\Gamma_1^{(1)}$	0	$-0.45206(\|{}^3\mathrm{H}_{44}\rangle+\|{}^3\mathrm{H}_{4\text{-}4}\rangle)+0.2230(\|{}^3\mathrm{H}_{42}\rangle+\|{}^3\mathrm{H}_{4\text{-}2}\rangle)+0.6412\|{}^3\mathrm{H}_{40}\rangle$ $+0.1711\|{}^3\mathrm{F}_{40}\rangle$
$\Gamma_2^{(1)}$	88	$-0.5343(\|{}^3\mathrm{H}_{43}\rangle+\|{}^3\mathrm{H}_{4\text{-}3}\rangle-0.4220(\|{}^3\mathrm{H}_{41}\rangle+\|{}^3\mathrm{H}_{4\text{-}1}\rangle)$
$\Gamma_1^{(2)}$	273	$-0.1943(\|{}^3\mathrm{H}_{44}\rangle+\|{}^3\mathrm{H}_{4\text{-}4}\rangle)-0.6435(\|{}^3\mathrm{H}_{42}\rangle+\|{}^3\mathrm{H}_{4\text{-}2}\rangle)+0.1675\|{}^3\mathrm{H}_{40}\rangle$
$\Gamma_3^{(1)}$	335	$0.6498(\|{}^3\mathrm{H}_{44}\rangle-\|{}^3\mathrm{H}_{4\text{-}4}\rangle)+0.2921\|{}^3\mathrm{H}_{50}\rangle+0.2108\|{}^3\mathrm{F}_{30}\rangle$
$\Gamma_4^{(1)}$	569	$0.1447(\|{}^3\mathrm{H}_{55}\rangle+\|{}^3\mathrm{H}_{5\text{-}5}\rangle)+0.3671(\|{}^3\mathrm{H}_{43}\rangle-\|{}^3\mathrm{H}_{4\text{-}3}\rangle)-0.1128(\|{}^3\mathrm{F}_{33}\rangle+\|{}^3\mathrm{F}_{3\text{-}3}\rangle)-0.5661(\|{}^3\mathrm{H}_{41}\rangle-\|{}^3\mathrm{H}_{4\text{-}1}\rangle)$
$\Gamma_4^{(2)}$	749	$-0.5778(\|{}^3\mathrm{H}_{43}\rangle-\|{}^3\mathrm{H}_{4\text{-}3}\rangle)+0.1489(\|{}^3\mathrm{H}_{53}\rangle+\|{}^3\mathrm{H}_{5\text{-}3}\rangle)-0.3368(\|{}^3\mathrm{H}_{41}\rangle-\|{}^3\mathrm{H}_{4\text{-}1}\rangle)+0.1143(\|{}^3\mathrm{F}_{31}\rangle+\|{}^3\mathrm{F}_{31}\rangle)$
$\Gamma_2^{(2)}$	1030	$0.4317(\|{}^3\mathrm{H}_{43}\rangle+\|{}^3\mathrm{H}_{4\text{-}3}\rangle)-0.1351(\|{}^3\mathrm{H}_{53}\rangle-\|{}^3\mathrm{H}_{5\text{-}3}\rangle)+0.1248(\|{}^3\mathrm{F}_{33}\rangle-\|{}^3\mathrm{F}_{3\text{-}3}\rangle)-0.4995(\|{}^3\mathrm{H}_{41}\rangle+\|{}^3\mathrm{H}_{4\text{-}1}\rangle)$
$\Gamma_1^{(3)}$	1685	$-0.4564(\|{}^3\mathrm{H}_{44}\rangle+\|{}^3\mathrm{H}_{4\text{-}4}\rangle)+0.1385(\|{}^3\mathrm{F}_{44}\rangle+\|{}^3\mathrm{F}_{4\text{-}4}\rangle)-0.6915\|{}^3\mathrm{H}_{40}\rangle-0.1458\|{}^3\mathrm{F}_{20}\rangle+0.1390\|{}^3\mathrm{F}_{40}\rangle$
$\Gamma_3^{(2)}$	2235	$0.6650(\|{}^3\mathrm{H}_{42}\rangle-\|{}^3\mathrm{H}_{4\text{-}2}\rangle)-0.1305(\|{}^3\mathrm{F}_{22}\rangle-\|{}^3\mathrm{F}_{2\text{-}2}\rangle)-0.1576(\|{}^3F_{42}\rangle-\|{}^3\mathrm{F}_{4\text{-}2}\rangle)$

[a] The admixtures of the ${}^{2S+1}L_J$ terms below 0.1 not shown.

$\chi_b(T)$ at $T\sim 200$ K. On the other hand, such a situation may promote a long range order of induced moments. According to the estimates by Wang and Cooper [65], the exchange integral J_x between the pseudospins induced on the uranium atoms should amount at least to $\Delta_{\mathrm{CF}}/(4|\langle 1|J_x|2\rangle|^2)\sim 22$ K, where Δ_{CF} is the CF splitting between the two singlets. This is a threshold of the exchange energy above which an ordered moment different from zero might appear at $T=0$ K. Apparently the uranium atoms being separated by 0.5184 nm are too distant to reach the above threshold value since the magnetic order is not observed in this compound down to the lowest temperature measured. Therefore, the molecular field shift has to be equal to zero, i.e., neither $\chi_i(0)$ nor the C constant in Fig. 6 are modified by the molecular shift (see Ref. [66]).

3. *Thermal properties*

The specific heat data $C_p(T)$ of $\mathrm{UFe_2Al_{10}}$ and the reference compound $\mathrm{ThFe_2Al_{10}}$, both measured from 2 to 300 K, are shown in Fig. 8 As this figure illustrates, these curves present the lack of any type anomaly associated with some kind of ordering in the whole temperature range measured. Practically no change has also been observed in $C_p(T)$ of the U-based aluminide in applied fields up to 9 T and at temperatures measured up to 50 K. The electronic specific heat constants $\gamma(0)$ and the Debye temperatures Θ_{D} were found for $B=0$ in a usual way from a least-squares fit of the C/T vs T^2 data as shown in the upper inset of Fig. 8. Unfortunately, there is rather a small temperature range where these data follow straight lines. The extrapolation to $T=0$ K yields $\gamma(0)\approx 28(1)$ and $18(2)\,\mathrm{mJ\,mol^{-1}\,K^{-2}}$ for the U- and Th-based aluminides, respectively. An almost parallel behavior of both straight lines yields close to each other values of Θ_{D}, which roughly is equal to 400(30) K. This fact is probably a consequence of that the lattice contributions for both these ternaries are almost the same, since these two phases have the same crystal structure and negligibly different lattice parameters, having also the same valence 4+ and mass difference of only 0.94%.

In the lower inset of Fig. 8 we have plotted the magnetic part of the specific heat which is obtained by subtracting the specific heat of $\mathrm{ThFe_2Al_{10}}$ from that of $\mathrm{UFe_2Al_{10}}$. An excess $\Delta C_p(T)$ found from this subtraction, we have roughly treated as the Schottky-like contribution due to the CF effect acting on the $\mathrm{U^{4+}}$ ion in the latter compound taking the CF level scheme given in Fig. 6(b). This excess, however, is very tiny in comparison to the whole specific heat values of the molecule containing 13 atoms, which becomes especially important at higher temperatures, where such a relative smallness leads to a considerable increase of the experimental error. Hence, we were able to obtain some reasonable results only up to 250 K. Any better determination of this excess would require us to perform much more precise measurements on purer materials. Despite these difficulties, the obtained Schottky-type anomaly really exists and even fairly well match the theoretical curve based on the CF calculation presented above, using the following expression:

$$C_{\mathrm{Sch}}(T)=\frac{R}{T^2}\left[\frac{\sum_i E_i^2 e^{-E_i/T}}{\sum_i e^{-E_i/T}}-\left(\frac{\sum_i E_i e^{-E_i/T}}{\sum_i e^{-E_i/T}}\right)^2\right],\qquad(2)$$

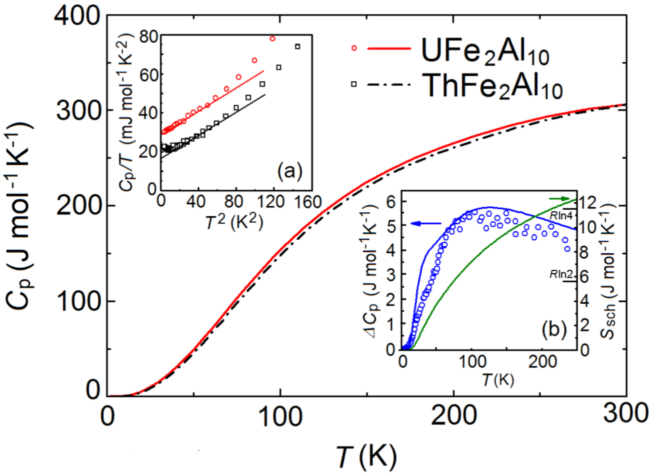

FIG. 8. (Color online) The specific heat of $\mathrm{UFe_2Al_{10}}$ and $\mathrm{ThFe_2Al_{10}}$ measured up to RT. Inset (a) shows the corresponding C_p/T vs T^2 curves, and inset (b) illustrates the theoretical and experimental Shottky-type contributions to the specific heat of the U-based aluminide. Note this inset presents also its calculated temperature change of magnetic entropy.

where summation runs over nine eigenvalues E_i (R is the universal gas constant).

In the same inset we have plotted the magnetic entropy which smoothly increases to a value slightly above $R\ln 4$ at 250 K.

C. Transport properties

1. Electrical resistivity

We have here a particular interest to study the transport properties of a rare metallic system among uranium intermetallics which shows simultaneously significant crystalline-field effects. Moreover, the ground and all excited states are nonmagnetic singlets which, however, do not give rise to an induced magnetic state down to the lowest measured temperatures [65]. Thus, in Fig. 9 we have plotted the electrical resistivity ρ_i against temperature T measured for a single crystal $\mathrm{UFe_2Al_{10}}$ with the current applied along the three axes: $i = a,b$, and c. As seen, all these curves have similar shapes of a rapidly increasing resistivity above 50 K, then undergoing through an inflection point T_{inf} at about 75−80 K [maxima in the temperature derivative $d\rho_i(T)/dT$, not shown here]. Finally, at temperatures above 150 K one observes a strong tendency to saturation for $\rho_a(T)$ and $\rho_b(T)$ or keeping a small slope ($d\rho/dT > 0$) along $\rho_c(T)$. All these three curves exhibit small anisotropy mainly due to the different values of the residual resistivity ρ_{i0}. In the inset to Fig. 9, the low-temperature ρ_i vs T^2 functions are plotted. As this inset indicates, the Fermi liquid behavior along all three crystallographic directions is followed by the particular resistivities, but above about 12 K, while below this temperature a small deviation from linearity of this function is observed, probably caused by impurities. As also evidenced in Fig. 9, the residual resistivity ratio (RRR) for the measured single crystals is rather low, only amounting to about 10.

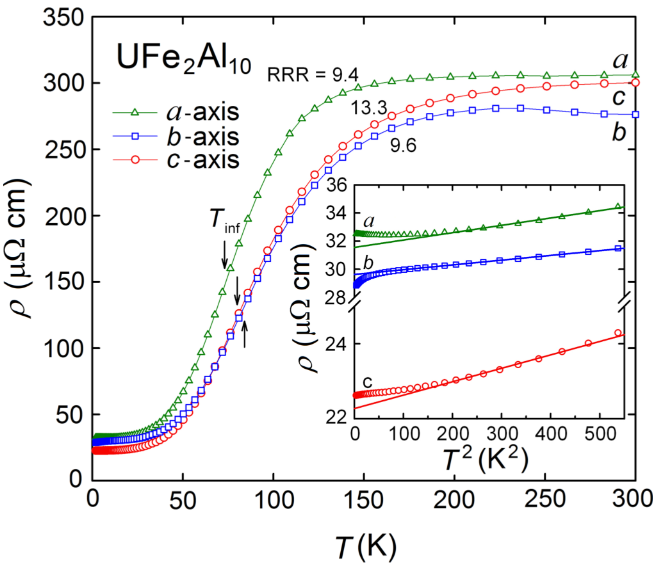

FIG. 9. (Color online) The electrical resistivity of $\mathrm{UFe_2Al_{10}}$ as a function of temperature measured along the three main crystallographic axes. The inset: ρ_i versus T^2. Note the Fermi liquid behavior above 12 K.

The observed shape of the $\rho_i(T)$ function of $\mathrm{UFe_2Al_{10}}$ is reminiscent of those measured for several intermetallic compounds containing the $\mathrm{Pr^{3+}}$ ions, isoelectronic to $\mathrm{U^{4+}}$, like in cubic $\mathrm{(Pr,La)Sn_3}$ [67] and $\mathrm{PrIn_3}$ [68] or hexagonal $\mathrm{PrCu_5}$ and orthorhombic $\mathrm{PrCu_6}$ [69], all these systems showing no magnetic ordering down to the lowest temperature measured. A good quantitative agreement between theory and experiment was obtained for all these examples of the singlet ground state systems after subtraction of a phonon component from their total resistivities using the data of corresponding isostructural nonmagnetic counterparts. It is then clear that the dramatic jump in the resistivity is unrelated to any magnetic order but can be explained by the inelastic scattering on crystal field levels. Unfortunately, the phonon contribution has not been taken into account in our data because of the lack of such data for the isostructural $\mathrm{ThFe_2Al_{10}}$. We can however say in advance that at least for the a and b axes, any consideration of the phonon contribution would cause the high temperature slope becoming distinctly $d\rho/dT < 0$. However, it can hardly be considered as a Kondo effect in the singlet CF ground state materials. On the other hand, it has been demonstrated [70] that the competition between the CF and exchange interactions (though being below a critical threshold) in a singlet ground CF system, as, e.g., is $\mathrm{PrIn_3}$, treated in a framework of the random phase approximation (RPA), can manifest itself as a flat resistivity maximum in $\rho_i(T)$ further followed by a negative slope. It turns out that such a behavior depends only on a combination of two parameters: the Fermi energy E_{F} and parameter A describing the ratio of the exchange J_{x} to CF splitting Δ_{CF}, as defined in Sec. IV B 2. Besides, as demonstrated in Sec. IV A 1, $\mathrm{UFe_2Al_{10}}$ exhibits also metallic properties due to a significant c-f hybridization, which probably arises mainly from so-called *dualism* of the $5f$ electrons (see, e.g., Refs. [50,56]). Such a state is characterized by the presence of both localized $5f^2$ electrons (being under the CF interactions) and also $5f6d$ hybridized orbitals forming with the ligand electrons a conduction band. It just underlines the fact of a metallic behavior of $\mathrm{UFe_2Al_{10}}$. Hence, one expects that the measured resistivity of such an intermetallic compound as is $\mathrm{UFe_2Al_{10}}$ consists of several different contributions which at present cannot be separated.

In view of the mixed-state metal with the singlet scheme of CF levels in $\mathrm{UFe_2Al_{10}}$, it was interesting to perform transverse magnetoresistance (TMR) measurements over a wide range of temperatures and magnetic fields. Figure 10 presents the relative TMR of $\mathrm{UFe_2Al_{10}}$ {defined as $[\Delta\rho/\rho(0)] = [\rho(B) - \rho(0)]/\rho(0)]$}, measured up to 9 T at several selected temperatures from 2 to 100 K and taken for the current directions along the three main crystallographic axes and perpendicular to the applied magnetic fields.

For all these three cases $\Delta\rho/\rho(0)_i$ is positive (except those at higher temperatures along $i = b$ and c) and has a parabolic character. It varies versus magnetic field as $\Delta\rho/\rho(0)_i = A_i(T)B^n$, where $1 < n < 2$ and its total value depends on temperature. In the insets to Figs. 10(a)–10(c) we have plotted the $A_i(T)$ functions, for $i = a,b$, and c. From these insets, it is apparent that $A_i(T)$ decreases smoothly with increasing temperature for the case of $j||a$, while for $j||b$ this decrease is faster at low temperatures and then continues smoothly. Unexpectedly, the behavior for $j||c$ is quite different, because

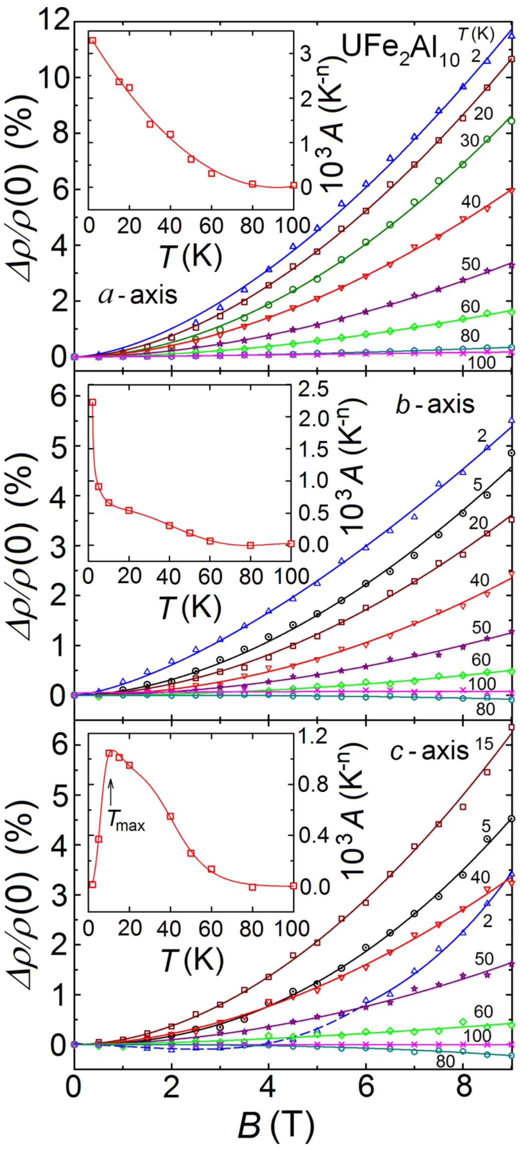

FIG. 10. (Color online) The transverse magnetoresistivity of UFe_2Al_{10} as a function of the magnetic field strength, measured along the three main crystallographic axes and at several selected temperatures. Insets: Temperature dependencies of A_i coefficients.

the $A_c(T)$ coefficient first starts with a sharp increase, goes through a maximum at $T_{max} \approx 10$ K, and then drops smoothly to zero at 100 K, as is the case along the other directions. The behavior for $i = a$ and b is reminiscent of a typical metallic character as that found recently in the fully metallic UB_{12} [71]. Also, the A coefficient for UB_{12} changes smoothly with temperature as does $A_a(T)$ and becomes close to zero near 100 K. The difference appears only in the $\Delta\rho/\rho(0)$ values achieved at 9 T and, e.g., at 2 K: for UFe_2Al_{10} these values are considerably lower than that in UB_{12}, which may be clarified if one compares the electronic structures of these two different metals (for UB_{12} see Ref. [72]). Another matter is the appearance of a distinct TMR anisotropy in here considered ternary aluminide, well seen in Fig. 11, in which we present the thermal behavior of TMR (open small symbols) taken at 9 T for single crystalline samples. At the same time, we have put on these smoothed curves the results obtained at 9 T from Fig. 10 (closed large symbols). As seen, both kinds of measurements are in good agreement. Again the $\Delta\rho/\rho(0)_i$ versus T curves (shown in this figure and measured for $i = a$ and b cases) decreases smoothly like that in UB_{12} [71], while the curve for $i = c$ goes through a diffuse maximum at $T_{max} = 19$ K. One should remember, however, that UFe_2Al_{10}, except a positive metallic contribution to the total TMR, brings in also a negative contribution arising from the attempts by an applied field to put some order among the spin-disordered paramagnetic moments. Alternatively, a large negative contribution may originate, e.g., from magnetic fluctuations (see, e.g., Ref. [73]). Inspecting the magnetic data of $CeRu_2Al_{10}$ we know that despite an easy a axis in the paramagnetic state, this compound has an antiferromagnetic transition with moments ordered just along the c axis [74]. We may have a similar situation like that in the Ce-aluminide but without setting a magnetic order. Hence, we can speculate that although a magnetic ordering in UFe_2Al_{10} has not been detected, there are possible magnetic fluctuations along the c axis signalizing a closeness to a critical point just proper for this direction. This is also based on the observation that the conflict described above does not exist in a TMR behavior of URu_2Al_{10} [75], where the c axis in the paramagnetic state is in contrast to UFe_2Al_{10}, an easy one as reported also in Ref. [10].

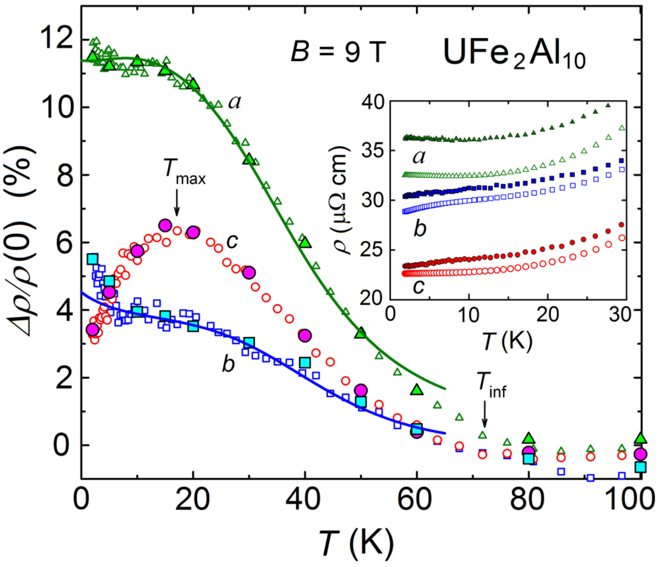

FIG. 11. (Color online) The transverse magnetoresistivity of UFe_2Al_{10} as a function of temperature along the three crystallographic axes. Solid lines denote fittings to Eq. (3) (in the range 2–60 K) with parameters a $= 0.486$ and 1.88 $[T^2(\mu\Omega\,cm)^{-1}]$, b $= -0.107$ and -0.438 for a and b axes, respectively. The inset: Low-temperature dependencies of the electrical resistivity ρ_i measured at 0 (open) and 9 T (closed symbols).

As Fig. 11 indicates, the $\Delta\rho/\rho(0)_i$ versus T dependencies (where $i = a$ and b) taken at 9 T for UFe_2Al_{10} can be fitted fairly well (but only at low temperature range) to Eq. (3) (solid lines):

$$\frac{\Delta\rho}{\rho(0)} = \frac{B^2}{\mathrm{a}[\rho(0,T)] + \mathrm{b}B^2}, \tag{3}$$

where a and b are the field- and temperature-independent parameters, depending exclusively on conduction electron properties, and $\rho(0,T)$ is the total resistivity at zero field. Because of an increasing temperature effect of the negative spin-disorder contribution, the upturn deviation of the fitted function takes place already above 50 K as shown in Fig. 11. The above formula describes the so-called *normal magnetoresistance*, i.e., the influence of the magnetic field on the conduction electron trajectories (so-called Lorentz effect). This mechanism always gives rise to positive TMR, whose magnitude increases while lowering the temperature at a fixed finite field. This effect is due to the simultaneous decrease of the electron-phonon scattering [73] which always falls when the temperature is decreased. The derived parameters from Eq. (3) are given in the caption to Fig. 11. As mentioned above, the observed maximum for $i = c$ is the result of an interplay between the negative and positive parts of the total TMR at low temperatures. To clarify this, however, a more sophisticated investigation is required. On the other hand, the observed anisotropy in the temperature variation of TMR for the presently studied aluminide seems to be caused by the c-f hybridization which becomes anisotropic in a similar way to that found for example for the isomorphic $\mathrm{CeFe_2Al_{10}}$ [76]. This compound is categorized as an intermediate-valence compound and, hence, has a nonmagnetic ground state. It was deduced for this material that the c-f hybridization is large in the ac plane but very small along the b axis.

2. *Thermoelectric power*

The thermoelectric power (TEP) $S_i(T)$ of $\mathrm{UFe_2Al_{10}}$, measured along the three main crystallographic axes, is displayed in Fig. 12. As seen, these temperature dependent curves are either positive (for S_b) or negative (for S_a and S_c) in the whole measured temperature range, i.e., from 0.4 to 300 K. Furthermore, a broad corresponding maximum appears at $T_{\max} \approx 75,70$, and 70 K for the b, a, and c axes, respectively. $S_b(T)$ after reaching a pronounced positive maximum with a value of $21\,\mu\mathrm{V\,K^{-1}}$ starts to decrease smoothly down to about $2\,\mu V\mathrm{K}^{-1}$ at RT. It appears that the temperature variations of the negative components, i.e., $S_a(T)$ and $S_c(T)$, are somehow different. The former achieves first a flat negative maximum of $-11\,\mu\mathrm{V\,K^{-1}}$ and then goes through a negative minimum at $T_{\min} \approx 110$ K, while the latter after going through a pronounced negative maximum with a value of $-28\,\mu\mathrm{V\,K^{-1}}$, exhibits then a much extended negative minimum at $T_{\min} \approx 200$ K reaching there a value of $-18\,\mu\mathrm{V\,K^{-1}}$. Finally, both curves coincide to a value of about $-22\,\mu\mathrm{VK^{-1}}$ at RT. It is interesting to note that there exists a certain similarity of our TEP data to those reported for $\mathrm{CeFe_2Al_{10}}$ [76]. In turn we have plotted in the inset to Fig. 12 the low temperature $S_i(T)$ curves as measured for the three crystal axes to present a way of their achieving the zero value. As this inset indicates, the zero value is approximately achieved by this function already at about $T \approx 0.4$ K. Hence, one can conclude that there exists some probability of occurring a superconducting state in $\mathrm{UFe_2Al_{10}}$ just below this temperature. Furthermore, by the solid curves we have marked in Fig. 12 the calculated crystal field contribution to the thermoelectric power, according to the fitting procedure by applying the Eq. (4) proposed by Fulde and Peschel [77]:

$$S(T) = S_d(T) + S_{\mathrm{CF}}(T) = AT + \mathrm{const.} \times F(T/\delta), \qquad (4)$$

where S_d and S_{CF} are two main contributions to the total TEP, i.e., the diffused and CF-effect ones, respectively. $A = \xi\pi^2 k_{\mathrm{B}}^2/eE_{\mathrm{F}}$, when ξ is the thermoelectric parameter depending on the mechanism of the electron scattering. The $F(T/\delta)$ is a universal function with a maximum at $T_{\max} \approx 0.3\delta$, δ being the energy distance between the ground and first excited CF levels. The fitting parameters are listed in Table V. As is clear from Fig. 12, the fitting curves (solid lines) reproduce quite well all the observed anomalies in the $S_i(T)$ curves. The derived energy splitting between the ground and the first excited CF level corresponds in our case not to an energy separation of two but rather it comprises three of the lowest lying levels. In Eq. (4) the possible presence of the phonon drag (S_g) has been omitted. However, similar maxima as one observes in $S_i(T)$ for $\mathrm{UFe_2Al_{10}}$ can also originate from such a phonon-drag contribution. Then their anisotropic behavior can be explained by distinct anisotropy of our Fermi surface (see Fig. 3) as that discussed in Ref. [78] (see Figs. 2.5 and 2.9 therein). However, to explain this behavior quantitatively, further calculations including electron-phonon interactions at the Fermi surface for different directions would be required, which is beyond the scope of this paper.

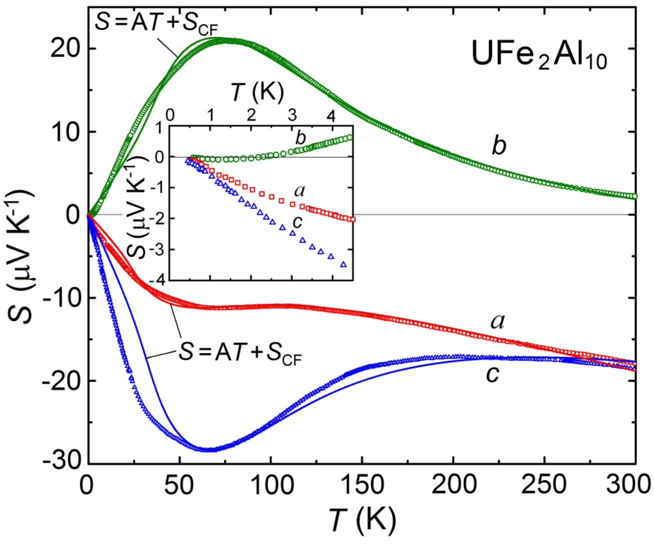

FIG. 12. (Color online) The thermoelectric power of $\mathrm{UFe_2Al_{10}}$ as a function of temperature measured along the three crystallographic directions. Solid lines denote fits of Eq. (4) to $S_i(T)$ data with parameters given in Table V. The inset: Low-temperature thermopower S_i.

TABLE V. Parameters of fits of Eq. (4) to thermoelectric power $S_i(T)$ data.

Axis	A_i ($\mu\mathrm{V\,K^{-2}}$)	Constant ($\mu\mathrm{V\,K^{-1}}$)	δ (K)
a	−0.0608	−9.17	184
b	−0.0085	25.17	279
c	−0.0562	−30.84	201

V. CONCLUSIONS

We have examined the UFe_2Al_{10} ternary uranium aluminide with a cage-type structure. It can be regarded simultaneously as a metallic system and a Van Vleck paramagnet without a tendency to magnetic ordering down to the lowest studied temperature of 0.4 K. These features have been concluded based on XPS and a set of bulk measurements performed on single-crystalline samples of that compound. We also performed both the band structure and crystal field potential calculations. The XPS valence spectrum showed two components of the $5f$-electron states, one located around E_F, and the other in the deeper binding energy scale. The former state being itinerant was well reproduced by band structure calculations, while the latter localized state was confirmed by CF potential calculations resulting in establishing the scheme of CF levels enabled to recreate the strong anisotropy in the temperature variation of the magnetic susceptibility as well as the Schottky-type data. We have applied in such calculations the intermediate coupling method in which all types of interactions are treated on an equal footing, i.e., the approach is much in demand in the case of CF probing any uranium compound. Besides the magnetic and specific heat results, we carried out also the electron transport measurements as temperature dependencies of the electrical resistivity (from 0 up to 9 T) and thermoelectric power. The evolution of the temperature dependence of the resistivity suggests clearly a domination of the CF effect on its shape. In addition, we attained a further confirmation of the *dual* character of the $5f$ electrons in UFe_2Al_{10} by analyzing also the transverse magnetoresisistivity and Seebeck coefficient results presenting the domination of either itinerant or localized behaviors of these electrons, respectively.

ACKNOWLEDGMENTS

We are grateful to H. Schilder for adapting his computer program Condon and kind support. The Computing Center at the Institute of Low Temperature and Structure Research of Polish Academy of Sciences in Wrocław is acknowledged for the use of the supercomputers and technical support.

---

[1] A. P. Gonçalves and H. Noël, Intermetallics **13**, 580 (2005).

[2] J. Stępień-Damm, A. Baran, and W. Suski, J. Less-Common Met. **102**, L5 (1984).

[3] M. Kuznietz, A. P. Gonçalves, J. C. Waerenborgh, M. Almeida, C. Cardoso, M.-M. Cruz, and M. Godinho, Phys. Rev. B **60**, 9494 (1999).

[4] L. Meshi, V. Y. Zenou, V. Ezersky, A. Munitz, and M. Talianker, J. Alloys Compd. **347**, 178 (2002).

[5] H. Noël, A. P. Gonçalves, and J. C. Waerenborgh, Intermetallics **12**, 189 (2004).

[6] L. Meshi, M. Talianker, and A. Munitz, J. Alloys Compd. **370**, 206 (2004).

[7] S. Niemann and W. Jeitschko, Z. Kristallogr. **210**, 338 (1995).

[8] V. Y. Zenou, L. Meshi, and D. Fuks, Intermetallics **19**, 713 (2011).

[9] L. Halevy, V. Y. Zenou, S. Salbov, E. N. Caspi, W. Schäfer, and I. Yaar, J. Alloys Compd. **419**, 21 (2006).

[10] T. Sugai, Y. Haga, T. D. Matsuda, E. Yamamoto, N. Tateiwa, F. Honda, R. Settai, and Y. Ōnuki, J. Phys.: Conf. Ser. **273**, 012122 (2010).

[11] T. Nishioka, Y. Kawamura, T. Takesaka, R. Kobayashi, H. Kato, M. Matsumara, K. Kodama, K. Matsubayashi, and Y. Uwatoko, J. Phys. Soc. Jpn. **78**, 123705 (2009); S. Kimura, T. Iizuka, H. Miyazaki, T. Hajiri, M. Matsunami, T. Mori, A. Irizawa, Y. Muro, J. Kajino, and T. Takabate, Phys. Rev. B **84**, 165125 (2011), and references therein.

[12] V. M. T. Thiede, T. Ebel, and W. Jeitschko, J. Mater. Chem. **8**, 125 (1998).

[13] Y. Muro, K. Motoya, Y. Saiga, and T. Takabatake, J. Phys. Soc. Jpn. **78**, 083707 (2009).

[14] S. C. Chen and C. S. Lue, Phys. Rev. B **81**, 075113 (2010).

[15] Y. Muro, K. Motoya, Y. Saiga, and T. Takabatake, J. Phys.: Conf. Ser. **200**, 012136 (2010).

[16] T. Takesaka, K. Oe, R. Kobayashi, Y. Kawamura, T. Nishioka, H. Kato, M. Matsumura, and K. Kodama, J. Phys.: Conf. Ser. **200**, 012201 (2010).

[17] H. Tanida, Y. Nonaka, D. Tanaka, M. Sera, Y. Kawamura, Y. Uwatoko, T. Nishioka, and M. Matsumura, Phys. Rev. B **85**, 205208 (2012).

[18] P. Khuntia, A. Strydom, F. Steglich, and M. Baenitz, Phys. Status Solidi B **250**, 525 (2013).

[19] A. M. Strydom, P. Peratheepan, R. Sakar, M. Baenitz, and F. Steglich, J. Phys. Soc. Jpn. **80**, SA043 (2011).

[20] X. Zhang, K. Feng, D. Wu, Y. Yang, P. Zheng, J. Yao, Y. Matsushita, A. Sato, H. Jiang, H. Wang, Y. Shi, K. Yamaura, and N. Wang, Inorg. Chem. **53**, 4387 (2014).

[21] P. Khuntia, A. M. Strydom, L. S. Wu, M. C. Aronson, F. Steglich, and M. Baenitz, Phys. Rev. B **86**, 220401 (2012).

[22] K. Park, L. S. Wu, Y. Janssen, M. S. Kim, C. Marques, and M. C. Aronson, Phys. Rev. B **84**, 094425 (2011).

[23] R. Troć, M. Pasturel, O. Tougait, M. Potel, and H. Noël, Intermetallics **19**, 913 (2011).

[24] M. Samsel-Czekała, E. Talik, M. Pasturel, and R. Troć, J. Alloys Compd. **554**, 438 (2013).

[25] G. Zwicknagl, A. N. Yaresko, and P. Fulde, Phys. Rev. B **65**, 081103(R) (2002); P. Thalmeier, Eur. Phys. J. B **27**, 29 (2002); A. Yaouanc, P. Dalmas de Réotier, P. C. M. Gubbens, C. T. Kaiser, A. A. Menovsky, M. Mihalik, and S. P. Cottrell, Phys. Rev. Lett. **89**, 147001 (2002); M. Dressel, N. Kasper, K. Petukhov, B. Gorshunov, G. Grüner, M. Huth, and H. Adrian, *ibid.* **88**, 186404 (2002).

[26] S. Tougaard, J. Electron Spectrosc. Relat. Phenom. **52**, 243 (1990).

[27] S. Doniach and M. Šunjić, J. Phys. C **3**, 285 (1970).

[28] R. Wawryk and Z. Henkie, Philos. Mag. B **81**, 223 (2001).

[29] FPLO-5.00-18 and 5.10-20; K. Koepernik and H. Eschrig, Phys. Rev. B **59**, 1743 (1999); http://www.FPLO.de; H. Eschrig, M. Richter, and I. Opahle, in *Relativistic Electronic Structure*

Theory, Part 2. Applications, edited by P. Schwerdtfeger, *Theoretical and Computational Chemistry*, Vol. 14 (Elsevier, Amsterdam, 2004), p. 723.
[30] J. P. Perdew and Y. Wang, Phys. Rev. B **45**, 13244 (1992).
[31] J. J. Yeh and I. Lindau, At. Data Nucl. Data Tables **32**, 1 (1985).
[32] A. Grassmann, Physica B **163**, 547 (1990).
[33] J.-S. Kang, J.-G. Park, K. A. McEwen, C. G. Olson, S. K. Kwon, and B. I. Min, Phys. Rev. B **64**, 085101 (2001); J.-S. Kang, S. C. Wi, J. H. Kim, K. A. McEwen, C. G. Olson, J. H. Shim, and B. I. Min, J. Phys.: Condens. Matter **16**, 3257 (2004).
[34] W. J. L. Buyers and T. M. Holden, in *Handbook on the Physics and Chemistry of the Actinides*, edited by A. J. Freeman and G. H. Lander (Elsevier Science, Amsterdam, 1985), Vol. 2, p. 239; M. J. Bull, K. A. McEwen, R. Osborn, and R. S. Eccleston, Physica B **223-224**, 175 (1996).
[35] K. A. McEwen, M. N. J. Bull, and R. S. Eccleston, Physica B **281/282**, 600 (2000).
[36] M. Samsel-Czekała, M. Werwiński, A. Szajek, G. Chełkowska, and R. Troć, Intermetallics **19**, 1411 (2011).
[37] J. A. Morkowski, G. Chełkowska, M. Werwiński, A. Szajek, R. Troć, and C. Neise, J. Alloys Compd. **509**, 6994 (2011).
[38] A. Szajek, J. A. Morkowski, A. Bajorek, G. Chełkowska, and R. Troć, J. Magn. Magn. Mater. **281**, 281 (2004).
[39] M. F. Beaux II, T. Durakiewicz, L. Moreschini, M. Grioni, F. Offi, G. Monaco, G. Panaccione, J. J. Joyce, E. D. Bauer, J. L. Sarrao, M. T. Butterfield, and E. Guziewicz, Electron Spectrosc. Relat. Phenom. **184**, 517 (2011).
[40] Y. Baer, H. R. Ott, and K. Andres, Solid State Commun. **36**, 387 (1980).
[41] E. Talik, M.-E. Lucas, W. Suski, and R. Troć, J. Alloys Compd. **350**, 72 (2003).
[42] T. Gouder, L. Havela, M. Diviŝ, J. Rebizant, P. M. Oppeneer, and M. Richter, J. Alloys Compd. **314**, 7 (2001).
[43] J. W. Allen, J.-S. Kang, Y. Lassailly, M. B. Maple, M. S. Torikachvili, W. Ellis, B. Pate, and I. Lindau, Solid State Commun. **61**, 183 (1987).
[44] T. Eijma, S. Suzuki, S. Saito, N. Saito, S. Fujimori, M. Yamada, K. Sato, T. Komatsubara, T. Kasuya, Y. Tezuka, S. Shin, and T. Ishii, J. Phys. Soc. Jpn. **63**, 2428 (1994).
[45] S. Fujimori, Y. Saito, N. Sato, T. Komatsubara, S. Suzuki, S. Sato, and T. Ishii, Solid State Commun. **105**, 185 (1998).
[46] M. Diviŝ, M. Richter, H. Eschrig, and L. Steinbeck, Phys. Rev. B **53**, 9658 (1996); T. Honma, Y. Inada, R. Settai *et al.*, J. Phys. Soc. Jpn. **69**, 2647 (2000).
[47] H. E. Fischer, E. T. Swartz, R. O. Pohl, B. A. Jones, and J. W. Wilkins, and Z. Fisk, Phys. Rev. B **36**, 5330 (1987).
[48] For example, P. Santini and G. Amoretti, Phys. Rev. Lett. **73**, 1027 (1994).
[49] K. Hanzawa, J. Phys. Soc. Jpn. **81**, 114713 (2012); **84**, 024717 (2015).
[50] R. Troć, Z. Gajek, A. Pikul, H. Misiorek, E. Colineau, and F. Wastin, Phys. Rev. B **88**, 024416 (2013).
[51] P. Santini, G. Amoretti, and A. Blaise, J. Appl. Phys. **73**, 6560 (1993).
[52] A. Grauel, A. Böhm, H. Fischer, C. Geibel, R. Köhler, R. Modler, C. Schank, F. Steglich, G. Weber, T. Komatsubara, and N. Sato, Phys. Rev. B **46**, 5818 (1992).
[53] B. Chevalier, R. Pöttgen, D. Darriet, P. Gravereau, and J. Etourneau, J. Alloys Compd. **233**, 150 (1996).
[54] Z. Gajek, J. Phys.: Condens. Matter **12**, 415 (2000).
[55] J. Mulak and Z. Gajek, *The Effective Crystal Field Potential* (Elsevier, Amsterdam, 2000).
[56] R. Troć, Z. Gajek, and A. Pikul, Phys. Rev. B **86**, 224403 (2012).
[57] M. Gerloch, J. H. Harding, and G. Wooley, Struct. Bonding **46**, 1 (1981).
[58] B. G. Wybourne, *Spectroscopic Properties of Rare Earths* (Wiley, New York, 1965).
[59] The program CONDON is free software, covered by the GNU General Public License, and is available from:http://www.condon.fh-aachen.de.
[60] H. Schilder and H. Lueken, J. Magn. Magn. Mater. **281**, 17 (2004).
[61] H. Schilder (private communication).
[62] A. P. Pikul, D. Kaczorowski, Z. Gajek, J. Stępień-Damm, A. Ślebarski, M. Werwiński, and A. Szajek, Phys. Rev. B **81**, 174408 (2010).
[63] Z. Gajek, Phys. Rev. B **72**, 045139 (2005).
[64] Z. Gajek, J. Phys. Chem. Solids **82**, 21 (2015).
[65] Y.-L. Wang and B. R. Cooper, Phys. Rev. **172**, 539 (1968).
[66] J. Mulak, J. Less-Comm. Met. **121**, 141 (1986).
[67] A. I. Abou Aly, S. Bakanowski, N. F. Berk, J. E. Crow, and T. Mihalisin, Phys. Rev. Lett. **35**, 1387 (1975).
[68] Z. Kletowski and P. J. Markowski, Solid State Commun. **62**, 299 (1987).
[69] S. Takayanagi, J. Phys. Soc. Jpn. **53**, 676 (1984).
[70] A. E. Szukiel, P. J. Markowski, and K. Durczewski, Phys. Status Solidi (b) **147**, 321 (1988).
[71] R. Troć, R. Wawryk, A. Pikul, and N. Shitsevalova, Philos. Mag. B **95**, 2343 (2015).
[72] M. Samsel-Czekała, E. Talik, R. Troć, and N. Shitsevalova, J. Alloys Compd. **615**, 446 (2014).
[73] E. Gratz and Markosyan, J. Phys.: Condens. Matter **13**, R385 (2001).
[74] A. Kondo, K. Kindo, K. Kunimori, H. Nohara, H. Tanida, M. Sera, R. Kobayashi, T. Nishioka, and M. Matsumura, J. Phys. Soc. Jpn. **82**, 054709 (2013).
[75] R. Troć *et al.* (to be published).
[76] H. Tanida, M. Nakamura, M. Sera, A. Kondo, K. Kindo, T. Nishioka, and M. Matsumura, J. Phys. Soc. Jpn. **83**, 084708 (2014).
[77] P. Fulde and I. Peschel, Adv. Phys. **21**, 1 (1972).
[78] F. J. Blatt, P. A. Schroeder, C. L. Foiles, and D. Greig, *Thermoelectric Power of Metals* (Plenum, New York, 1976), pp. 29 and 36.